TiO₂/guar gum hydrogel composite for adsorption and photodegradation of methylene blue

Shella Permatasari Santoso [a,b,*], Artik Elisa Angkawijaya [c], Vania Bundjaja [b], Chang-Wei Hsieh [d], Alchris Woo Go [c], Maria Yuliana [a], Hsien-Yi Hsu [e,f], Phuong Lan Tran-Nguyen [g], Felycia Edi Soetaredjo [a,b], Suryadi Ismadji [a,b]

[a] Chemical Engineering Department, Faculty of Engineering, Widya Mandala Surabaya Catholic University, Jl. Kalijudan No. 37, Surabaya 60114, East Java, Indonesia
[b] Chemical Engineering Department, National Taiwan University of Science and Technology, #43 Keelung Rd., Sec. 4, Da'an Dist., Taipei 10607, Taiwan
[c] Graduate Institute of Applied Science and Technology, National Taiwan University of Science and Technology, #43 Keelung Rd., Sec. 4, Da'an Dist., Taipei 10607, Taiwan
[d] Department of Food Science and Biotechnology, National Chung Hsing University, No. 145 Xingda Road, 402, South District, Taichung City, Taiwan
[e] School of Energy and Environment, Department of Materials Science and Engineering, City University of Hong Kong, 83 Tat Chee Ave, Kowloon Tong, Hong Kong, China
[f] Shenzhen Research Institute of City University of Hong Kong, Shenzhen 518057, China
[g] Mechanical Engineering Department, Can Tho University, 3/2 Street, Ninh Kieu Dist., Can Tho City, Viet Nam

ARTICLE INFO

ABSTRACT

The development of porous adsorbent materials from renewable resources for water and wastewater treatment has received considerable interest from academia and industry. This work aims to synthesize composite hydrogel from the combination of guar gum (a neutral galactomannan polysaccharide) and TiO₂. The TiO₂-embedded guar gum hydrogel (TiO₂@GGH) was utilized to remove methylene blue through adsorption and photodegradation. The presence of TiO₂ particles in the hydrogel matrix (TiO₂@GGH) was confirmed by scanning electron microscopy-energy dispersive X-ray and X-ray photoelectron spectroscopy analysis. The mercury intrusion and N₂ sorption isotherm indicate the macroporous structure of the TiO₂@GGH composite, showing the presence of pore sizes ~420 μm. The dye removal efficiency of the GGH and TiO₂@GGH was evaluated in batch mode at ambient temperature under varying pH. The effect of UV radiation on the dye removal efficiency was also assessed. The results demonstrated that the highest dye removal was recorded at pH 10, with the equilibrium condition achieved within 5 h. UV radiation was shown to enhance dye removal. The maximum adsorption capacity of TiO₂@GGH is 198.61 mg g⁻¹, while GGH sorbent is 188.53 mg g⁻¹. The results imply that UV radiation gives rise to the photodegradation effect.

1. Introduction

The contamination in water bodies by non-hazardous and hazardous wastes is a persistent problem in transition and developing countries [1,2]. While water contamination by solid wastes can easily be managed through simple separation processes (e.g., filtration and sedimentation); however, leachate from solid wastes has a high probability of being released into water bodies during their residence time in the water. Leachates often contain various soluble organic and inorganic compounds, thus requiring a more complex treatment to remove them from water bodies [3]. Dyes are among the many types of soluble substances often found to contaminate water bodies. In addition to their vast array of variety, properties, and toxicities, the high solubility of dyes in water increases the complexity of their handling. The content of the polar chromophoric groups in the dye structure contributes to their water binding ability and color transmission to water bodies (and/or other substrates, such as aquatic organisms) [4,5]. Besides disturbing the aesthetics of water bodies, these colors may block the penetration of sunlight and oxygen into the water. As a result, the balance of living aquatic biota can be disturbed; for instance, the photosynthesis of aquatic plants becomes hindered due to the absence of a light source. In addition, dyes are known to have mutagenic and carcinogenic properties

that can harm the surrounding biota. Dyes are also known to increase the levels of chemical oxygen demand (COD) compounds which can dramatically reduce dissolved oxygen levels in water [6–10].

Azo dyes are the highly utilized dyes for the textile coloring processes. However, less than 50% of the dye molecules are bound to the textiles, and the remainder is discharged as wastewater [9,11,12]. Often, these dye-contaminated wastewaters were directly discharged to water bodies without any pretreatment [4] or utilized for irrigating agricultural fields [13]. The usage of this dye-containing water for irrigation may cause a detrimental effect on the growth of soil-fertilizing microorganisms and drive impaired growth of the plants [14]. Due to the detrimental effect of dyes, various types of sorbents have been developed for their removal from water bodies. The removal of dye by sorbent occurs through multiple processes, such as adsorption, photodegradation, biodegradation, biosorption, and absorption [15]. Biodegradation and biosorption by utilizing microorganisms can be considered an eco-friendly process; however, they require a long time (i. e., 40–60 h) to proceed, depending on the strain of the microorganisms. Another limitation of the microorganism-involving process is that it can only be applied for a low concentration of dyes since a high concentration of dyes can be toxic to the microorganisms and inhibit their growth [16–18]. Adsorption is considered the most promising initial step to reduce the high level of dye contamination. Adsorbent material used in an adsorption process often can also have absorption ability [19,20]. The development of sorbents from biomass (including microorganisms and plant-based materials) is swiftly done as an effort to create eco-friendly materials [21,22].

In this work, a plant polysaccharide (i.e., guar gum, GG) is chosen as the raw material for the preparation of hydrogel adsorbents. GG is a neutral-hydrophilic galactomannan polysaccharide with (1–4)-linked-β-$_D$-mannopyranose backbone and (1–6)-linked- β-$_D$-galactopyranose branch at the 6th-positions. GG can be obtained from renewable resources, i.e., guar beans (*Cyamopsis tetragonoloba*), making it one of the sustainable polymers. The use of GG in the production of polysaccharide-based hydrogels has gained increasing interest, owing to its comparable properties to other polysaccharide-based hydrogels. In particular, GG-based hydrogels are postulated to possess a non-toxic nature, biodegradable, strong hydration rate, strong hydrogen bonding, good pH stability, high water solubility, and high porosity [23–26]. Despite its superior properties, only limited studies have reported the potential adsorption ability of GG. The most recent studies reported the utilization of GG/bentonite/*N,N*-methylenebisacrylamide composite hydrogel for Cr(IV) removal with adsorption capacity of 4.89–182.4 mg g^{-1} [27] and adsorption of U(VI) by phosphorylated GG/magnetite/chitosan with adsorption capacity of 1.16 mmol/g [28].

The adsorption performance of GGH and TiO$_2$-added GGH (TiO$_2$@GGH) was investigated against azo dye methylene blue (MB). Modification by the addition of TiO$_2$ particles was done to equip the GGH with photodegradation ability. MB is employed as the model azo dye due to its abundance in wastewater and its adverse effect on the living biota owing to its photo-reactivity properties [29,30]. This work is the first to report the adsorption and photodegradation ability of TiO$_2$@GGH. The detailed characterizations of GGH and TiO$_2$@GGH were performed using scanning electron microscopy-energy dispersive spectroscopy (SEM-EDS), N$_2$ sorption isotherm, mercury intrusion porosimetry (MIP), Fourier transform infrared (FTIR) spectroscopy, x-ray diffraction (XRD), thermogravimetric analysis (TGA), cyclic compression test, and x-ray photoelectron spectroscopy (XPS) to gain insight on their physicochemical properties. The influence of adsorption conditions, such as pH, salinity, adsorbent dosing, and adsorbate initial concentration, on the adsorption performance of GGH and TiO$_2$@GGH were evaluated. Furthermore, the kinetics and isotherm adsorption models were established to elucidate the adsorption mechanism of MB onto GGH and TiO$_2$@GGH adsorbent.

2. Materials and methods

2.1. Materials

Guar gum (GG) powder was obtained from Sigma Aldrich (Singapore). Sodium hydroxide (NaOH, 96% purity), urea (CH$_4$N$_2$O, 98% purity), methylene blue (C$_{16}$H$_{18}$ClN$_3$S, 85% dye content), TiO$_2$ (~325 mesh), and epichlorohydrin (C$_3$H$_5$ClO, 98% purity) were obtained from Merck (Germany). All chemicals were directly used as received without further purification. The water used to prepare the solutions were purified with a Millipore Milli-Q system (18.2 MΩcm).

2.2. Preparation of guar gum hydrogel (GGH)

GG solution was prepared by dissolving 3 g of GG powder into a solvent mixture prepared from 7 g NaOH, 12 g urea, and 81 g distilled water. The mixture was stirred for 30 min to obtain a transparent gel-like solution. Subsequently, 5 mL epichlorohydrin was added into the mixture, and the stirring was continued for another 30 min. The gel solution was then poured into a mold and steam-heated in a 60 °C water bath for 20 min. The resulting GG hydrogels (GGH) were washed by running tap water overnight to remove the excess reactants. The hydrogels were then collected and kept in a refrigerator before being used for later experiments.

2.3. Preparation of TiO$_2$@GGH

GG solution was prepared by dissolving 3 g of GG powder into a solvent mixture prepared from 7 g NaOH, 12 g urea, and 81 g distilled water. 30 mg of TiO$_2$ particle was added into GG solution before the addition of 5 mL epichlorohydrin. The mixtures were then poured into a mold and steam-heated in a 60 °C water bath for 20 min. The resulting TiO$_2$@GGH were washed in running tap water for overnight to remove the excess reactants. The hydrogels were collected and kept in a refrigerator before being used for further experiment.

2.4. Characterization

SEM analysis was performed using a JEOL JSM-7900F field emission SEM. The samples were freeze-dried prior to the analysis; a small fraction of the dried samples were then fixed onto a metallic holder using adhesive carbon tape. The samples were coated by a thin layer of Pt/Pd alloy using a fine auto-coater JEOL JEC-3000FC prior to the SEM imaging. N$_2$ sorption isotherm was performed at 77 K using a Quadrasorb SI analyzer. The samples were degassed at 423 K for at least 6 h before measurement. The porosity analysis was done by modeling the isotherm data using Bruneuer-Emmett-Teller (BET) model. MIP analysis was conducted with micromeritics AutoPore IV 9520. The XPS spectra of the BioMOFs were obtained by using Thermo Scientific VG ESCALAB 250 X-ray photoelectron spectrophotometer (XPS) and analyzed by using XPSPEAK41 software. XRD analysis was conducted using a Bruker D2 Phaser X-ray diffractometer with a CuKα radiation λ = 1.5418 Amstrong. FTIR analysis was performed using a Bio-Rad FTS-3500 GX at wavenumber range from 4000 to 400 cm^{-1}; the spectra were collected from 128 scans with a resolution of 4 cm^{-1}. TG/DTG analysis was conducted using a TA instrument TGA 550 at a temperature range of 30 to 600 °C. The compressive strength of the materials was analyzed by a Universal testing machine (UTM, Testometric M500-25AT/M500-25CT)

2.5. Adsorption and photodegradation study

The removal of MB from the solution was done by applying adsorption or photodegradation process. The adsorption process was done by introducing the prepared adsorbent into MB solutions. This mixture was then incubated for a certain period without ultraviolet (UV) radiation. Meanwhile, the photodegradation process was done similarly

Table 1
The mathematical expression of the kinetic and isotherm model.

Model	Equation	Parameter	Ref.
Kinetic model			
Pseudo-1st-order (P1O)	$Q_t = Q_1[1 - \exp(-k_1 t)]$	Q_1 = removal capacity (mg g^{-1})	[31]
		k_1 = removal rate (min^{-1})	
Pseudo-2nd-order (P2O)	$Q_t = Q_2\left(\dfrac{Q_2 k_2 t}{1 + Q_2 k_2 t}\right)$	Q_2 = removal capacity (mg g^{-1})	[32]
		k_2 = removal rate (g mg^{-1} min^{-1})	
Elovich	$Q_t = \dfrac{1}{\beta}\ln(1 + \alpha\beta t)$	α = initial adsorption rate (mg g^{-1} min^{-1})	[33]
		β = desorption constant (g mg^{-1})	
Intraparticle diffusion (IPD)	$Q_t = k_{IPD} t^{0.5} + C_i$	k_{IPD} = IPD rate constant (mg g^{-1} min$^{-0.5}$)	[34]
		C_i = arbitrary constant (mg g^{-1})	
Isotherm model			
Langmuir (L)	$Q_e = \dfrac{Q_L K_L C_e}{1 + K_L C_e}$	Q_L = removal capacity (mg g^{-1})	[35]
		K_L = Langmuir constant (L mg^{-1})	
Freundlich (F)	$Q_e = K_F C_e^{(1/n_F)}$	K_F = removal capacity (mg g^{-1}) (mg L^{-1})$^{-n}$	[36]
		n_F = dimensionless constant	
Sips (S)	$Q_e = \dfrac{Q_S a_S C_e^{s_p}}{1 + a_S C_e^{s_p}}$	Q_S = removal capacity (mg g^{-1})	[36]
		a_S = Sips constant (L mg^{-1})[a]	
		s_p = Sips exponent[a]	
Redlich-Peterson (RP)	$Q_e = \dfrac{K_{RP} C_e}{1 + a_{RP} C_e^{\beta}}$	K_{RP} = RP constant (L g^{-1})[b]	[36]
		a_{RP} = RP constant (L mg^{-1})[b]	
		β = RP exponent[c]	

[a] S model reduced to L as $s_p = 1$, and to F model as $a_S \to 0$.
[b] The ratio of K_{RP} to a_{RP} show the removal capacity ($Q_{RP} = K_{RP}/a_{RP}$).
[c] RP model reduced to L as $\beta = 1$, and to F model as $a_{RP} C_e^{\beta} > 1$.

to that of the adsorption process with the presence of UV radiation. The UV radiation was done by using UV light with radiation power of 145 μW.cm^{-2}. The adsorption and photodegradation study was performed at several modified parameters to investigate the effect of each parameter. The studied parameters are as follow:

(i) *Effect of pH*: A series of MB solutions with an initial concentration of 200 ppm and volume of 50 mL was prepared. A different amount of 0.15 M NaOH was added to adjust each solution pH to 3, 4, 5, 6, 7, 8, 9, 10, and 11. Subsequently, the adsorbent ($\pm$ 0.1 g) was added into the solutions, and the adsorption or photodegradation process was conducted for 10 h.

(ii) *Effect of salinity*: A series of MB solutions with an initial concentration of 200 ppm and volume of 50 mL was prepared at different salinity. The salinity of the solutions was adjusted by adding 300 ppm NaCl, 20 ppm Na$_2$CO$_3$, or 300/20 ppm NaCl/Na$_2$CO$_3$. The pH of the solutions was adjusted to a pH of 10, where the removal of MB was found to proceed optimally. Subsequently, the adsorbent ($\pm$ 0.1 g) was added into the solutions, and the adsorption or photodegradation process was conducted for 10 h.

(iii) *Kinetic study:* A series of MB solutions with an initial concentration of 200 ppm and volume of 50 mL was prepared. The adsorbent ($\pm$ 0.1 g) was then introduced into each solution. The residual concentration of MB was then measured at different periods.

(iv) *Isotherm study*: A series of MB solutions with various initial concentrations (up to 200 ppm) and volume of 50 mL was prepared. Subsequently, $\pm$ 0.1 g adsorbent was added into the solutions, and the adsorption or photodegradation process was conducted for 10 h.

(v) *Recyclability study*: Post-adsorption, the ± 0.1 g samples were immersed in 1 M HCl solution for 4 h. Then, the sample was washed using ethanol and water sequentially for three consecutive washings. The regenerated sample was then used in the next adsorption process.

The measurement of the residual concentration of MB in the bulk solution was determined using spectrophotometric measurement at a wavelength of 660 nm.

2.6. Data processing and modeling

The data obtained from the adsorption or photodegradation study was used to study the performance of GGH or TiO$_2$@GGH for MB removal. The %removal of MB was calculated according to Eq. (1).

$$\%\text{removal} = (C_i - C_f/C_i) \times 100 \qquad (1)$$

where C_i and C_f are the initial and final concentration of MB in the solution (mg L^{-1}).

The removal efficiency (%) was used to express the decrease in the % removal due to adsorption inhibiting factor (i.e., salt); it was calculated according to Eq. (2).

$$\%\text{removal efficiency} = (Q_{\text{salt}}/Q_{\text{control}}) \times 100 \qquad (2)$$

where Q_{salt} is the adsorption capacity in the presence of salt (mg g^{-1}), and Q_{control} is the adsorption capacity without the presence of salt (mg g^{-1}).

The kinetic study was conducted to determine the rate of adsorption or photodegradation according to Pseudo-1st-order (P1O), Pseudo-2nd-order (P2O), and Elovich model (see Table 1). Furthermore, the intraparticle diffusion (IPD) model was fitted to the data to elucidate the removal mechanism. The model fitting was done on the kinetic curves, which established by plotting the Q_t vs. t data; t is the adsorption or photodegradation time (min) and Q_t is the amount of MB adsorbed at a given period (mg g^{-1}). Q_t is determined according to Eq. (3).

$$Q_t = (C_i - C_t) \times m/V \qquad (3)$$

C_t is the MB concentration at a specific time (mg L^{-1}), m is the mass of adsorbent (g), and V is the volume of the system (L).

The isotherm study was conducted to give insight into the adsorption or photodegradation behavior. The isotherm modeling was done using several models, such as Langmuir, Freundlich, Sips, and Redlich-Peterson models (see Table 1). The model fitting was done on the plot of Q_e (the amount of MB removed (mg L^{-1})) vs. C_e (the equilibrium concentration of MB in the solution (mg L^{-1})). The value of Q_e was obtained according to Eq. (4).

$$Q_e = (C_i - C_e) \times m/V \qquad (4)$$

3. Results and discussion

3.1. Characterization of GGH and TiO$_2$@GGH

In this work, GGH was produced using epichlorohydrin as a chemical crosslinker, where the formation mechanism is illustrated in Fig. 1a. Given that the structure of GG is similar to that of other natural polysaccharides (e.g., cellulose), the mechanism of GGH formation is postulated to be identical to that of other polysaccharide-based hydrogels. In detail, the formation of GGH was initiated by dissolving GG powder in a solvent mixture of NaOH/urea. Here NaOH acts as a strong base that cleaves hydrogen bonding and induces the hydroxyl groups deprotonation of GG [44], thus facilitating GG dissolution. At the same time, the presence of urea can further promote GG dissolution by capping its hydrophobic moiety and allowing it to bind with water molecules. Thus, the hydrogen bond disrupted-GG can be readily
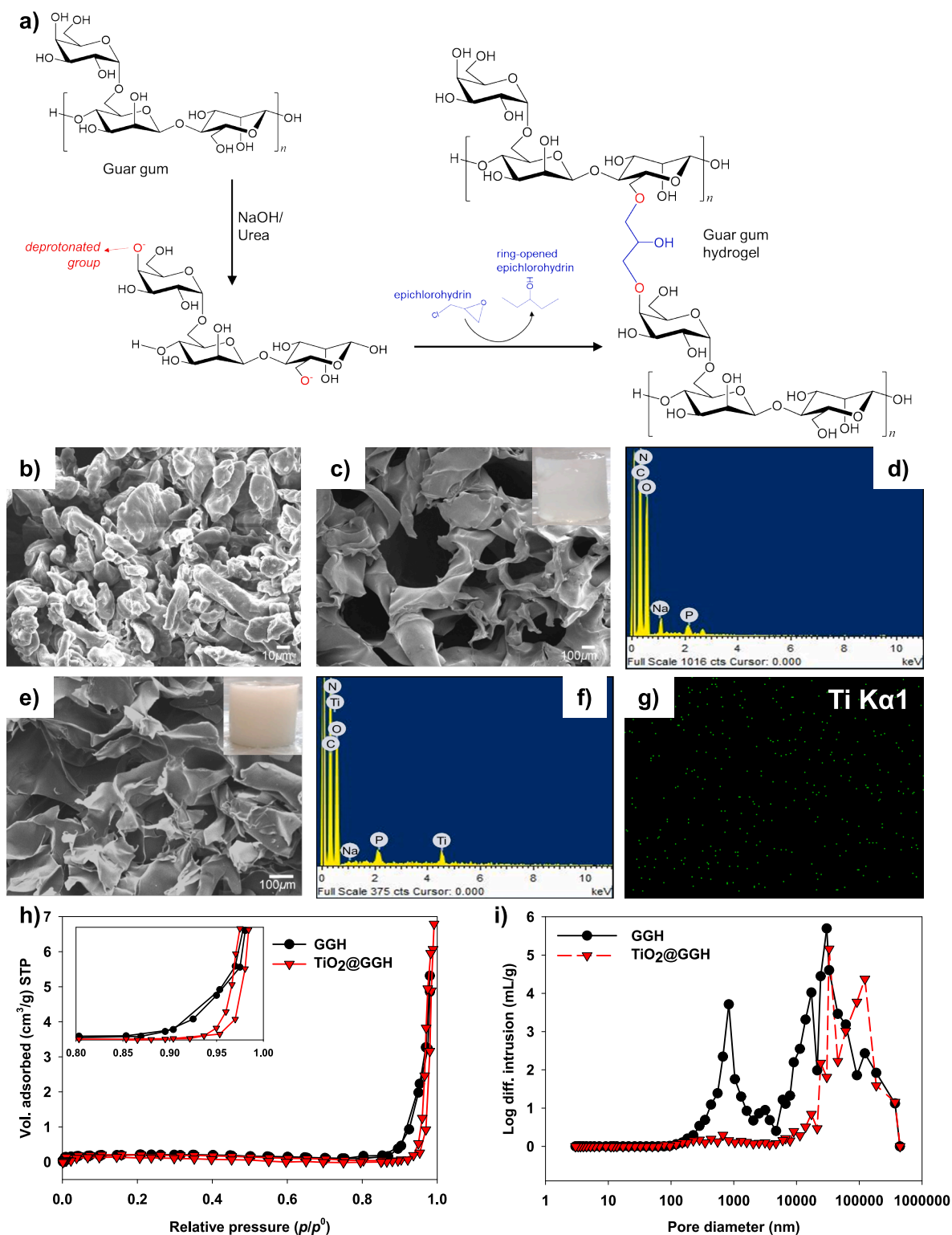
Fig. 1. (a) The formation mechanism of GGH. SEM images of (b) guar gum powder, (c) GGH, and (e)TiO$_2$@GGH. Energy dispersive spectra of (d) GGH, (f) TiO$_2$@GGH, and (g) elemental mapping of Ti on TiO$_2$@GGH. N$_2$ sorption isotherm (g) and MIP pore size distribution (h) of GGH and TiO$_2$@GGH.

crosslinked with the aid of epichlorohydrin. The occurrence of NaOH in this system was also postulated to act as the catalyst for the nucleophilic ring-opening of the epoxide group of epichlorohydrin [37–39]. These ring opened-epichlorohydrin then connects the two adjacent GG polymers by binding to their disrupted-hydroxyl groups. Upon heating, the GG polymers form aggregates that gelate in an aqueous solution [40] and eventually transform into a hydrogel. In the formation of

TiO$_2$@GGH, 30 mg of TiO$_2$ particles were added into the GG solution before adding epichlorohydrin. The viscous GG solution causes the TiO$_2$ particles to disperse uniformly in the solution, which eventually allows the TiO$_2$ particles to be captivated in-between the GG networks and uniformly distributed in GGH matrices upon hydrogel formation.

Fig. 1b, c, and e show the electron micrograph images of raw guar gum powder (GG), GGH, and TiO$_2$@GGH, respectively. The raw GG
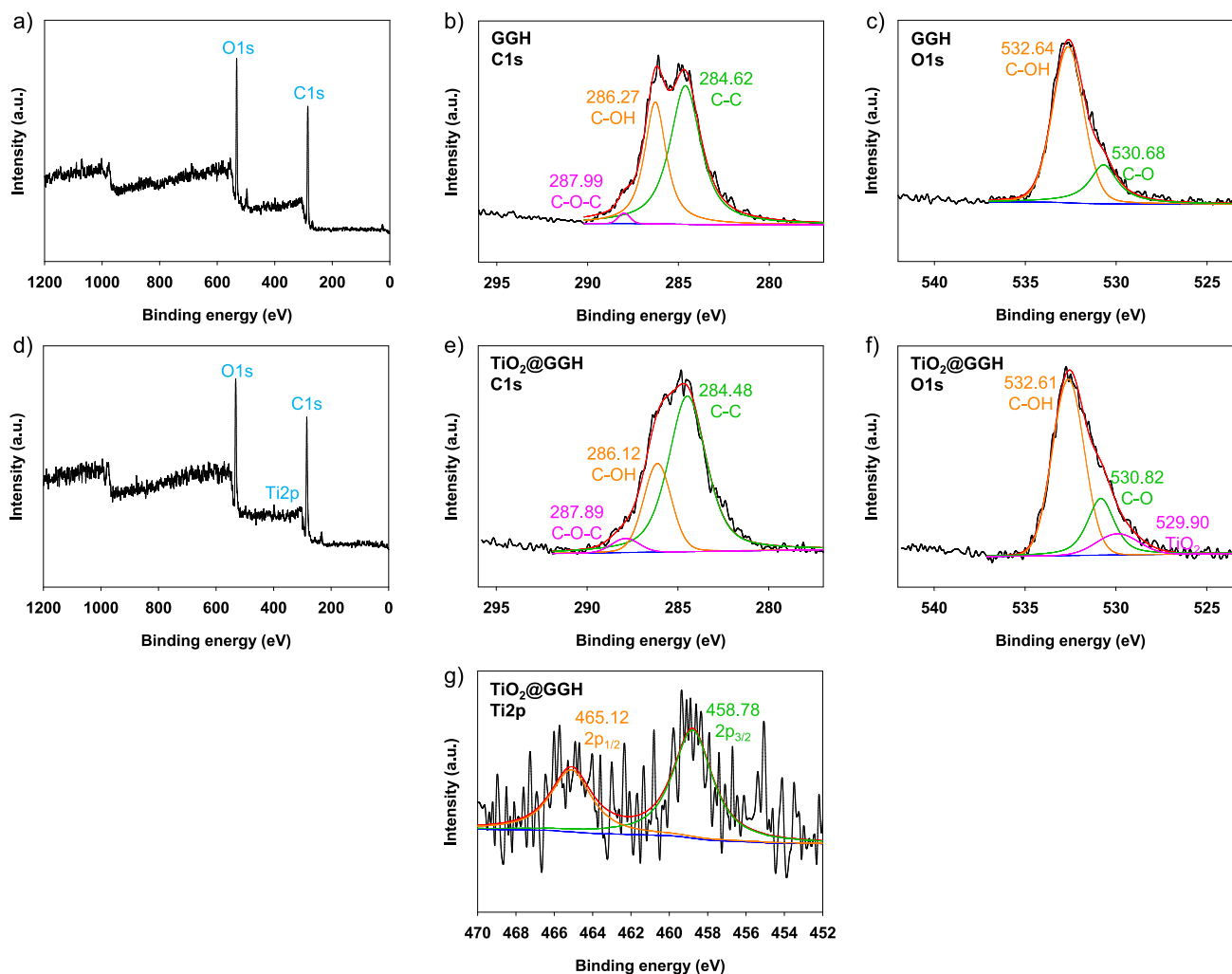
Fig. 2. XPS spectrum of (a) GGH and the corresponding deconvolution (b) C1s peak and (c) O1s peak. XPS spectrum of (d) TiO$_2$@GGH and the corresponding deconvolution (e) C1s peak, (f) O1s peak, and (g) Ti2p peak.

powder had an irregular granular shape which and each granule appeared in different sizes. The non-adherent granules indicate no hydrogen bonding between the particles [41]. Upon hydrogel formation (i.e., GGH), the GG particles were bound to each other and formed a sponge-like network (Fig. 1c). These networks generate cavities resembling large macropores with a diameter > 100 nm. The TiO$_2$@GGH (Fig. 1e) possess a similar structure as the GGH micrograph, indicating that TiO$_2$ addition did not significantly influence the GGH networking. The presence of TiO$_2$ particles appearance in TiO$_2$@GGH was confirmed by the appearance of Ti-peak in the energy-dispersive spectra of TiO$_2$@GGH (Fig. 1f) and the corresponding elemental mapping (Fig. 1g). The addition of TiO$_2$ particles altered the color of GGH from transparent to milky-white, as displayed in the inset photograph of Fig. 1c and e.

Fig. 1h shows the N$_2$ sorption isotherm curves of GGH and TiO$_2$@GGH; this method was employed to analyze the porosity characteristic of synthesized materials. According to the IUPAC classification, all samples display the Type II isotherm curve, which accounts for macroporous material. A marginal hysteresis loop was observed in the adsorption-desorption curve of TiO$_2$@GGH at high relative pressure > 0.8 (inset Fig. 1h), which can be associated with the filling-emptying of mesopores by capillary condensation; suggesting the minor relevance of mesopores. The non-horizontal isotherm at relative pressure close to 1 indicates a considerable population of macropores [37,38]. Thus, mercury intrusion porosimetry (MIP) analysis was conducted to evaluate the

Table 2
The atomic composition of GGH and TiO$_2$@GGH obtained by XPS analysis.

Atom	Atomic content (%)	
	GGH	TiO$_2$@GGH
C	73.55	70.24
O	25.06	27.31
N	1.40	2.10
Ti	–	0.35

macroporosity of the sample (Fig. 1i). The GGH pores were distributed around 0.2 to 5 μm and 5.5 to 420 μm; this distribution was narrowed to ~9 to 420 μm in the TiO$_2$@GGH sample. The pore size observed through the MIP method has a good agreement with that of pore size observed in the SEM images, which is greater than 100,000 nm (100 μm). The total intrusion volume of GGH and TiO$_2$@GGH is 6.78 and 4.11 cm^3/g, respectively; meanwhile, the total pore area is 9.13 and 2.17 m^2/g, respectively.

The XPS of GGH and TiO$_2$@GGH are shown in Fig. 2. The XPS spectra (Fig. 2a-f) revealed the dominance of C and O species at ~285 and 533 eV, respectively. The successful TiO$_2$ embedding was confirmed by the appearance of a deconvoluted peak at 530 eV (Fig. 2f), which corresponds to the lattice O and Ti^{4+} binding [42]. In addition, the occurrence of a typical Ti2p spectrum [42,43] with two peaks identified at 465 and 459 eV corresponding for Ti2p$_{1/2}$ and Ti2p$_{3/2}$ was also observed in
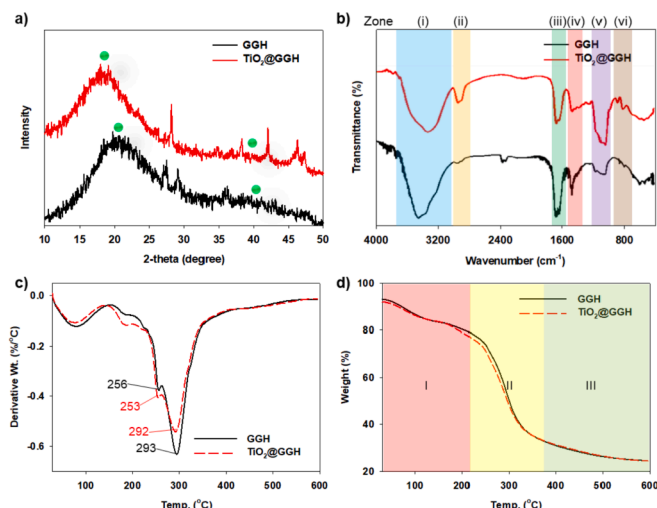
Fig. 3. (a) XRD pattern, (b) FTIR spectra, and (c, d) TGA/DTG curves of GGH and TiO₂@GGH.

TiO₂@GGH samples. The presence of TiO₂ in the TiO₂@GGH was also confirmed from its calculated atomic content, as summarized in Table 2.

Fig. 3a shows the XRD pattern of TiO₂, GGH, and TiO₂@GGH. GGH shows a broad reflection at 20.6° and a hump at 40.0° (as pointed by the green dots in Fig. 3a), which correspond to the amorphous phase of the guar gum. These scattering patterns are similar to native galactomannan spectra reported in several studies [44,45]. Those amorphous phase peaks were slightly shifted for TiO₂@GGH, specifically at 18.3° and 39.8°. FTIR spectra of GGH and TiO₂@GGH were presented in Fig. 3b. Some of the characteristic bands of TiO₂@GGH are similar to GGH but with a certain degree of shifting. In zone (i) – the band corresponds to the O—H stretching *vibration* was observed at 3426 cm^{-1} for GGH, this band was shifted to 3278 cm^{-1} ($\delta = 148$ cm^{-1}, δ is the magnitude of the change in wavenumber). The shift of the O—H group can be attributed to the interaction of this group with TiO₂ in the formation of TiO₂@GGH. In zone (ii) – band associated with C—H stretching vibration is found in similar wavenumber for GGH and TiO₂@GGH, respectively, at 2903 cm^{-1} and 2898 cm^{-1} ($\delta = 5$ cm^{-1}). In zone (iii) – the band corresponds to the C—C ring stretching vibration was found at 1631 cm^{-1} for GGH and was slightly shifted to 1608 cm^{-1} for TiO₂@GGH ($\delta = 23$ cm^{-1}). The C—H stretching band was found at 1566 cm^{-1} for GGH and 1562 cm^{-1} for TiO₂@GGH ($\delta = 4$ cm^{-1}). In zone (iv) – the appearance of the band at 1398 cm^{-1} for GGH was due to the CH₂ deformation; the band was observed at 1405 cm^{-1} for TiO₂@GGH ($\delta = 7$ cm^{-1}). In zone (v) – the band corresponds to C-O-C stretching vibration was rise at 1094 cm^{-1} and 979 cm^{-1} in GGH, the band was shifted to

1026 cm^{-1} ($\delta = 68$ cm^{-1}) and 961 cm^{-1} ($\delta = 18$ cm^{-1}) in TiO₂@GGH. In zone (vi) – the bands that indicate galactose and mannose groups were observed at 796 cm^{-1} and 736 cm^{-1} for GGH, which is in accordance with the reported FTIR of GG [46]; these bands were found at a similar wavenumber for TiO₂@GGH (i.e., 791 cm^{-1} and 731 cm^{-1}).

Fig. 3c and d show the TGA/DTG curves of GGH and TiO₂@GGH, where both samples displayed similar thermal degradation tendencies. The degradation stage of the samples can be divided into three regions. Region I was observed at a temperature range < 215 °C, where the minor mass loss occurred due to water evaporation. Region II, sharp weight reduction due to the degradation of GGH was found at the temperature range of 215–370 °C. The significant mass loss frequently occurred during oxidation, dehydration, hydrolysis, depolymerization, and decarboxylation of polysaccharide-based materials [47]. The thermal degradation was started at 230 °C with a minimal mass loss, followed by a more substantial degradation (~7% mass loss) at 256 °C for GGH or 253 °C for TiO₂@GGH. The highest degradation temperature (T$_d$) for GGH and TiO₂@GGH was found at 293 °C and 292 °C, where ~20% mass loss occurred. At higher temperatures, >370 °C, the thermal degradation rate for both samples slows down. The degradation at this last region occurred due to the graphitized guar gum polysaccharide, a common phenomenon in other polysaccharides such as cellulose [47,48]. The mass loss tends to be minimal at this stage. The mass residue of both samples was ~24% at 600 °C. The TGA analysis shows that the addition of TiO₂ does not positively nor adversely influence the thermal stability of GGH.

The deformation recoverability of GGH and TiO₂@GGH is observed over the five consecutive loading-unloading compressions of GGH and TiO₂@GGH. As shown in Fig. 4a and b, at all terminal strains (25%, 50%, and 75%), the five cycle hysteresis loops of TiO₂@GGH are almost overlapped. A minimal deviation of the GGH hysteresis loop of GGH can be observed upon cyclic compression at the terminal strain of 75%. Nevertheless, these results suggest that both samples have impressive deformation recoverability under a certain degree of compression.

3.2. Adsorption performance

3.2.1. Effect of pH on MB removal efficiency

The pH of the solution significantly influences the adsorption performance, affecting the charge of the adsorbate and adsorbent. There are two possible forms of MB when dissolved in an aqueous solution, that is the un-dissociated MB (zero charged, MB^0) and the dissociated MB (positively charged, MB$^+$). The presence of MB$^+$ is becoming more dominant than the MB^0 as the pH of the solution is >3.8, and MB$^+$ becomes the only species present in the solution at pH > 6 [49]. The surface charge distribution of the TiO₂@GGH sample was investigated by determining the point-of-zero-charge (Pzc) according to a previously published procedure [9,50]. The Pzc of TiO₂@GGH was found to be 7.5
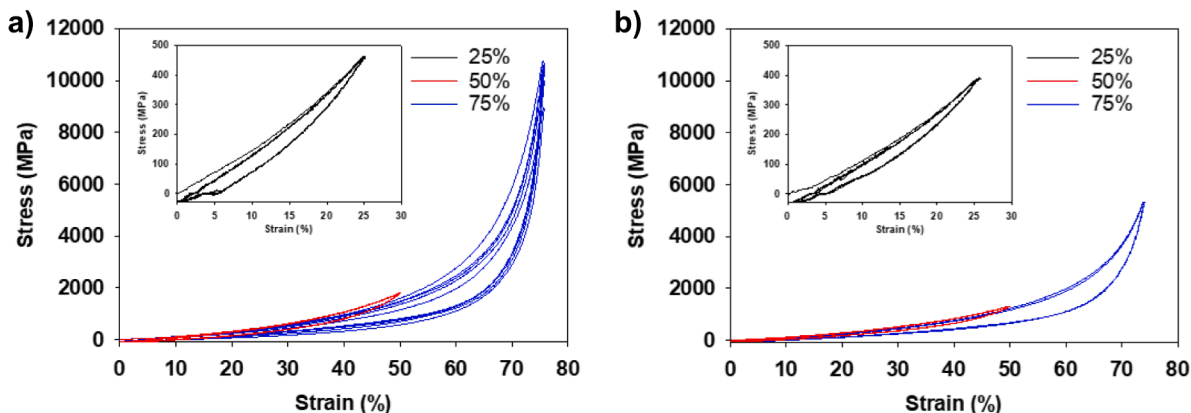

Fig. 4. Cyclic compression curves of GGH (a) and TiO₂@GGH (b) after five consecutive loading-unloading compression at various strains (25%, 50%, and 75%).
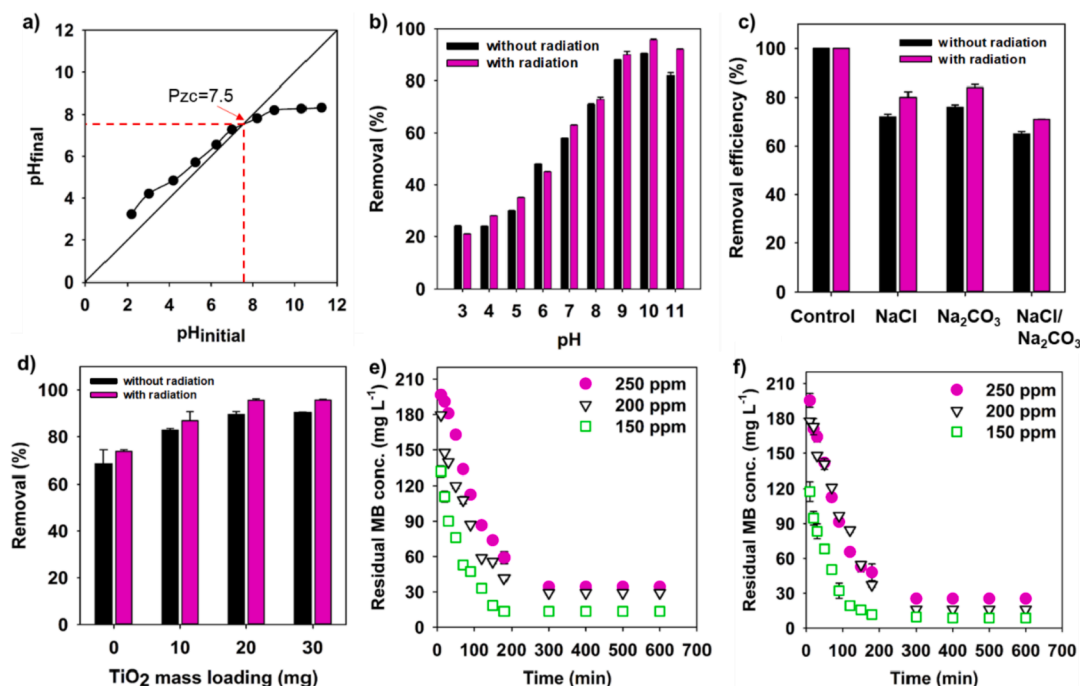
Fig. 5. (a) Point-of-zero-charge (Pzc) of TiO_2@GGH. The effect of different operating conditions on the removal of MB by TiO_2@GGH: (b) effect of pH, (c) the effect of salinity, (d) the effect of different TiO_2, (e) the effect of adsorbate dose without radiation, (f) the effect of adsorbate dose with radiation.

(Fig. 5a); TiO_2@GGH are positively charged as the pH < Pzc and negatively charged as pH > Pzc. According to their charge behavior, the adsorption of MB by TiO_2@GGH would occur better at alkaline pH (i.e., >7.5) —That is when the MB^+ molecules are more dominant, and the adsorbents have a negative surface charge.

Fig. 5b shows the effect of pH on the removal of MB by TiO_2@GGH. As expected, the removal of MB was lower at acidic pH and gradually increased as the solution pH became more alkaline —The phenomena were similar for MB removal with or without radiation. The highest MB removal occurred at a pH of 10, and it was lowered at a further pH increase. Since both have a positive charge, the repulsion interactions were more dominant at acidic pH between adsorbate and adsorbent. The surface charge of the adsorbent gradually becomes more negative at higher pH, which leads to the attractive forces between the adsorbent and the cationic MB. The decline in the adsorption occurs as the pH becomes more alkaline (i.e., >10), which can be attributed to the high number of oxyanions (OH^-). The OH^- may interact with the MB^+, and therefore, interrupting the interaction between MB^+ and the adsorbent [51].

3.2.2. Effect of salinity on MB removal efficiency

The effect of salinity was studied at a salt concentration of 300 ppm NaCl and/or 20 ppm Na_2CO_3; these conditions were chosen to mimic the typical salt concentration found in textile industry wastewater [9]. Fig. 5c shows the influence of salt on the removal of MB by TiO_2@GGH; it was also noted that radiation results in higher MB removal. The removal efficiency was decreased by: $16 \pm 1\%$ (with radiation) and $24 \pm 1\%$ (without radiation), at a given salt concentration of 20 ppm Na_2CO_3; $20 \pm 2\%$ (with radiation) and $28 \pm 1\%$ (without radiation), at a given salt concentration of 300 ppm NaCl; and, $29 \pm 0\%$ (with radiation) and $35 \pm 1\%$ (without radiation), at a given salt concentration of 20/300 Na_2CO_3/NaCl. The decline of MB removal in the presence of salt can be attributed to the attachment of salt cations (i.e., Na^+) onto the surface of the adsorbent; thus, the interaction of the adsorbent toward MB is disrupted.

3.2.3. Effect of different TiO_2 loading on MB removal efficiency

Fig. 5d shows the effect of different TiO_2 particles loading on the removal of MB molecules. The highest removal that can be achieved by GGH (with 0 mg TiO_2 loading) is $74 \pm 1\%$ (with radiation) and $69 \pm 1\%$ (without radiation). The addition of TiO_2 particles gives increase on the MB removal, that is: $87 \pm 4\%$ (with radiation) and $83 \pm 1\%$ (without radiation) at 10 mg TiO_2 addition; $96 \pm 1\%$ (with radiation) and $90 \pm 1\%$ (without radiation) at 30 mg TiO_2 addition. The MB removal does not increase significantly at higher TiO_2 addition (i.e., 50 mg), specifically $96 \pm 0\%$ (with radiation) and $91 \pm 0\%$ (without radiation). The higher TiO_2 loading provides more adsorption sites; thus, more MB molecules can be removed from the bulk solution. At a high TiO_2 loading (i.e., 50 mg), there is no significant increase —This phenomenon probably occurred because the number of TiO_2 particles on the surface of GGH was similar to the 30 mg TiO_2 loading. Some portions of TiO_2 particles might be infested far from the GGH surface; therefore, they have a lower affinity toward the adsorbate molecules.

3.2.4. Effect of contact time on MB removal

Fig. 5e and f show the decrease of MB concentration in bulk solution at a given time; the observation was done at different initial MB concentrations. The rapid decrease of MB concentration, which also signifies rapid removal, occurred during the first 200 min of the process; the equilibrium was reached gradually afterward, which was indicated by the insignificant increase of the removal. The rapid increase, in the beginning, happened since the active sites of the adsorbent were still vacant; thus, the adsorbate molecules were instantaneously adsorbed onto the adsorbent. The affinity was getting lower as most active sites interacted, and the removal rate was slowing down. In this stage, the adsorption of MB molecules mostly happens via the diffusion phenomena [9]. The equilibrium MB concentration at 600 min of the process is 25.364 ± 0.729 mg g^{-1} ($C_0 = 250$ ppm), 15.985 ± 1.307 mg g^{-1} ($C_0 = 200$ ppm), 8.667 ± 0.429 mg g^{-1} ($C_0 = 150$ ppm), in the presence of radiation; and, 34.364 ± 0.515 mg g^{-1} ($C_0 = 250$ ppm), 29.121 ± 0.043 mg g^{-1} ($C_0 = 200$ ppm), 13.439 ± 0.455 mg g^{-1} ($C_0 = 150$ ppm), in the absence of radiation. It was noted that the residual concentration of MB in the bulk solution is higher at higher C_0; this is since at higher C_0, the
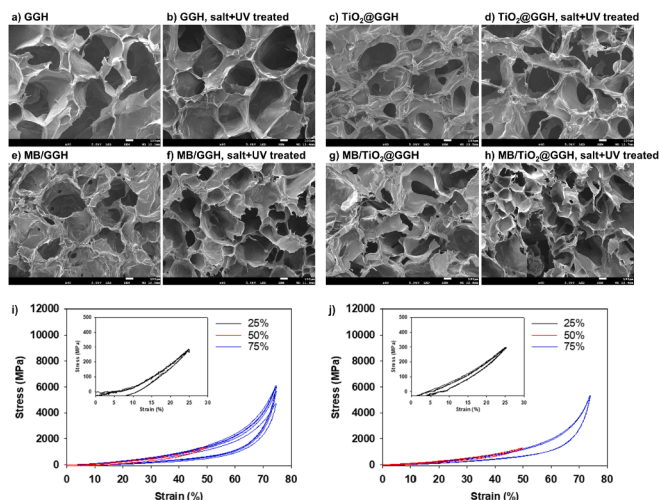
Fig. 6. The SEM morphology of (a) fresh and (b) salt+UV treated GGH, (c) fresh and (d) salt+UV treated TiO$_2$@GGH. Post MB-adsorption morphology of (e) GGH, (f) salt+UV treated GGH, (g) TiO$_2$@GGH, (h) salt+UV treated TiO$_2$@GGH. Cyclic compression curves of salt+UV treated (i) GGH and (j) TiO$_2$@GGH after five consecutive loading-unloading compression at various strains (25%, 50%, and 75%).

ratio of the initial number of MB molecules to the active adsorption sites is low, and therefore, the residual amount of MB remain in the solution is high [52].

3.2.5. Effect of salinity and UV-radiation on the physical properties of the adsorbent

The morphology and compression recoverability of the samples after immersion in salt-containing solution and UV-radiation was done to gain an insight into the physical properties of the hydrogels and evaluate their correlation with their adsorption performance. The morphology of GGH and TiO$_2$@GGH before and after MB-adsorption, with or without salt+UV treatment, was shown in Fig. 6a-h. No significant morphological alterations can be observed in all samples upon treatment with salt (20/300 ppm Na$_2$CO$_3$/NaCl) and UV radiation. This shows that the

reduced MB removal efficiency was not influenced by the physical properties of the adsorbent but caused by the occurrence of interfering salt ions. The five consecutive loading-unloading compression cycles of salt+UV treated GGH and TiO$_2$@GGH at different strains were presented in Fig. 6i and j, respectively. It can be seen that the salt+UV treated samples are less rigid compared to the untreated samples (refer to Fig. 4a and b). However, the hysteresis loop curves of the salt+UV treated samples are almost overlapped for each cycle; this shows that the samples still have an excellent deformation recoverability.

3.2.6. Kinetic study

A kinetic study was conducted to demonstrate the removal rate of MB by the investigated adsorbents. Fig. 7 shows the kinetic data curve of the removal of MB by GGH or TiO$_2$@GGH. After 600 min, the GGH adsorbent was able to remove 147.517 ± 0.684 mg of MB per g of the adsorbent in the presence of radiation and declined to 136.924 ± 5.987 mg g^{-1} in the absence of radiation. Similarly, for TiO$_2$@GGH adsorbent, the removal of MB was higher in the presence of radiation (191.182 ± 0.643 mg g^{-1}) than in the absence of radiation (179.015 ± 1.307 mg g^{-1}). This result indicated that the addition of TiO$_2$ could lead to the higher removal of MB. To predict the removal rate of MB by the synthesized adsorbent, the kinetic data were fitted against the P1O, P2O, and Elovich models. The data fitting can be seen in Fig. 7a and b, and the fitting parameters are given in Table 3. The P1O model could satisfy the kinetic data better than the P2O and Elovich models, indicating the higher R^2 value and lower RSS. Furthermore, the Q_1 of the P1O model has a similar value to that of Q_{exp}, which further confirmed that the P1O model could fit the kinetic data better. This result suggests that the physisorption may be dominant in the process; this argument is supported by the low congruency of the kinetic data with the Elovich model fitting [9].

The intraparticle diffusion (IPD) model was also employed to elucidate the removal mechanism of the investigated system. As shown in Fig. 7c and d, the systems have two to three linear segments. The value of the fitting parameters for the IPD model was summarized in Table 3. For the system involving GGH with radiation, GGH without radiation, and TiO$_2$@GGH without radiation, the first segment occurred at $t \leq 300$ min ($t^{0.5} \leq 17.32$ min$^{0.5}$), and the second segment occurred afterward. For the system of TiO$_2$@GGH with radiation, the first segment occurred
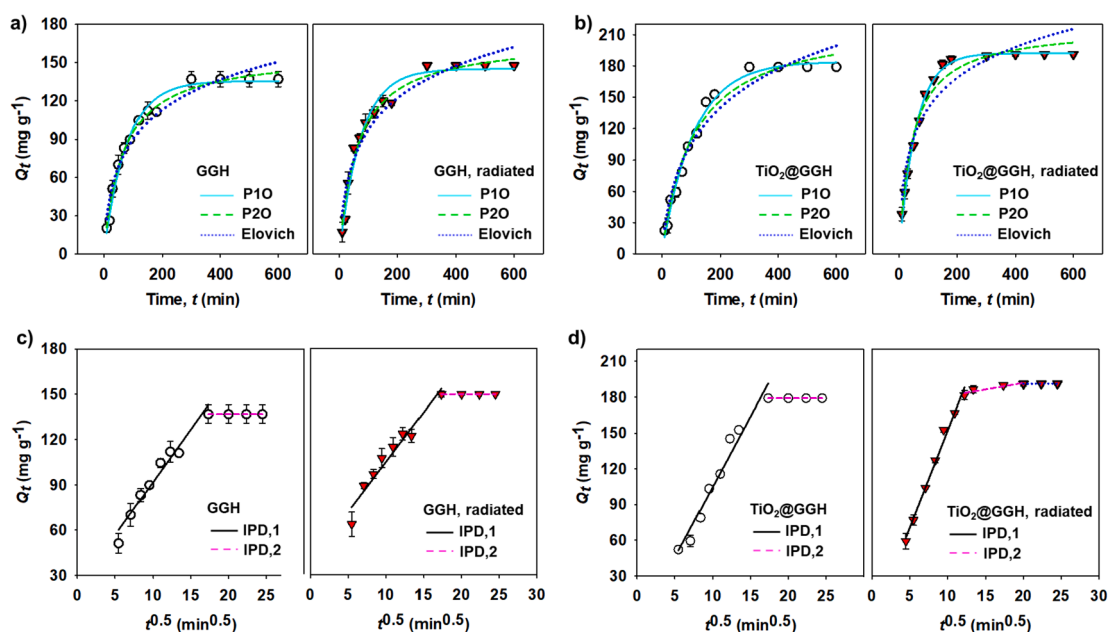

Fig. 7. (a) Removal kinetics and kinetic models fitting for adsorption of MB by GGH. (b) Intra-particle diffusion analysis for adsorption of MB by GGH. (c) Adsorption kinetics and kinetic models fitting for adsorption of MB by TiO$_2$@GGH. (d) Intra-particle diffusion analysis for adsorption of MB by TiO$_2$@GGH.

Table 3

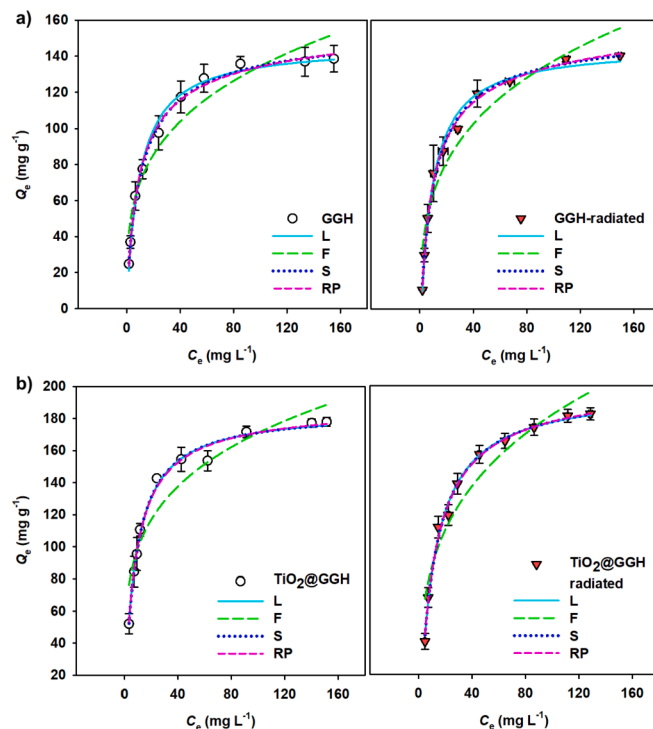The fitting of kinetic parameters for the MB removal by GGH and TiO₂@GGH.

Parameter	Unit	GGH		TiO₂@GGH	
		Without radiation	With radiation	Without radiation	With radiation
Q_{exp}[a]	mg g⁻¹	136.924 ± 5.987	147.517 ± 0.684	179.015 ± 1.307	191.182 ± 0.643
Pseudo-1st-order (P1O)					
Q_1	mg g⁻¹	135.455 ± 2.702	144.998 ± 3.590	184.195 ± 3.811	192.253 ± 1.952
k_1	min⁻¹	0.010 ± 0.001	0.013 ± 0.001	0.009 ± 0.001	0.017 ± 0.001
R^2[b]		0.987	0.984	0.989	0.994
RSS[c]		213.573	373.187	453.489	198.770
Pseudo-2nd-order (P2O)					
Q_2	mg g⁻¹	157.810 ± 3.822	168.661 ± 5.040	225.386 ± 10.225	238.100 ± 6.527
k_2 (×10⁵)	g mg⁻¹ min⁻¹	9.505 ± 0.001	9.486 ± 0.001	3.993 ± 0.001	7.240 ± 0.001
R^2[b]		0.987	0.980	0.974	0.971
RSS[c]		249.771	455.196	1041.872	1006.429
Elovich					
α	mg g⁻¹ min⁻¹	4.187 ± 0.036	4.650 ± 0.043	3.031 ± 0.017	4.568 ± 0.113
β	g mg⁻¹	0.028 ± 0.003	0.027 ± 0.004	0.017 ± 0.007	0.023 ± 0.006
R^2[b]		0.954	0.943	0.947	0.896
RSS[c]		875.883	1268.254	2097.102	3552.333
Intraparticle diffusion (IPD)					
First segment					
$C_{i,1}$	mg g⁻¹	21.908 ± 6.564	29.151 ± 7.733	13.370 ± 10.114	9.369 ± 6.779
$k_{IPD,1}$	mg h⁻¹ min¹ᐟ²	6.996 ± 0.591	7.060 ± 0.695	11.829 ± 0.923	16.392 ± 0.779
R^2		0.946	0.936	0.953	0.987
Second segment					
$C_{i,2}$	mg g⁻¹	136.924 ± 0.0.000	147.517 ± 0.000	179.015 ± 0.000	169.949 ± 5.184
$k_{IPD,2}$	mg h⁻¹ min¹ᐟ²	~0.000	~0.000	~0.000	1.101 ± 0.323
R^2		0.926	0.924	0.974	0.910
Third segment					
$C_{i,3}$	mg g⁻¹				191.182 ± 0.000
$k_{IPD,3}$[d]	mg h⁻¹ min¹ᐟ²				~0.000
R^2					1.0000

[a] Q_{exp} is the highest removal capacity based on the experimental data.
[b] R^2 is the adjusted R-squared of the data fitting.
[c] RSS is the residual sum of squares of the data fitting.
[d] Nearly zero value.

Fig. 8. Removal isotherm and isotherm-models fitting of MB by (a) GGH and (b) TiO₂@GGH in the presence and absence of radiation.

at $t \leq 120$ min ($t^{0.5} \leq 10.95$ min$^{0.5}$) of contact time, the second segment occurred at $120 > t \leq 300$ min (10.95 min$^{0.5} > t^{0.5} \leq 17.32$ min$^{0.5}$), and the third segment occurred afterward. The first segment is related to the instantaneous interaction between the adsorbate molecules with the active surface sites of the adsorbent; this segment is signified by the rapid increase of Q_t and high rate constant ($k_{IPD,1}$). The second segment is the equilibrium stage for the system of GGH with radiation, GGH without radiation, and TiO₂@GGH without radiation, which is indicated by the nearly zero rate constant ($k_{IPD,2}$). Meanwhile, for TiO₂@GGH with radiation, the equilibrium stage was reached at the third segment; at the second segment, the lower rate constant was due to the saturation of the active surface sites of the adsorbent and the increase of diffusion resistance [34].

3.2.7. Isotherm study

Fig. 8 shows the isotherm data of the MB removal by GGH or TiO₂@GGH at 30 °C; it can be noted that the removal of MB was found to be higher in the presence of radiation than without radiation. According to the adsorption isotherm classification, the isotherm curve shows an H-type isotherm with subclass 2 for all systems; this suggests that the interaction between the adsorbate and adsorbent was occurring via electrostatic interaction, and the interaction is more likely to be irreversible. The H-type isotherm curve is indicated by the $Q_e > 0$, even when the adsorbate concentration is zero. Subclass 2 indicates the absence of intermolecular interaction between the adsorbate molecules in the bulk solution and the adsorbed-adsorbate molecules. The system with subclass 2 commonly can be well-represented by the L model [53].

The L, F, S, RP model fitting is represented by the lines in Fig. 8a and b, and the fitting parameters are summarized in Table 4. It was noted that the systems were well convergent with the L model than the F model, which is indicated by the R^2 nearly 1.000 and low RSS. The Q_L value was also similar to that of Q_{exp}, which further confirmed the congruency of the data with the L model. The congruency of the data with the L model is also supported by the exponent parameter value of the S and RP model. The exponent of the S model (n_S) has a value close to 1; similarly, the exponent of the RP model (β) is also close to 1. This indicates the homogeneous adsorption behavior, which is in congruence with the L model.
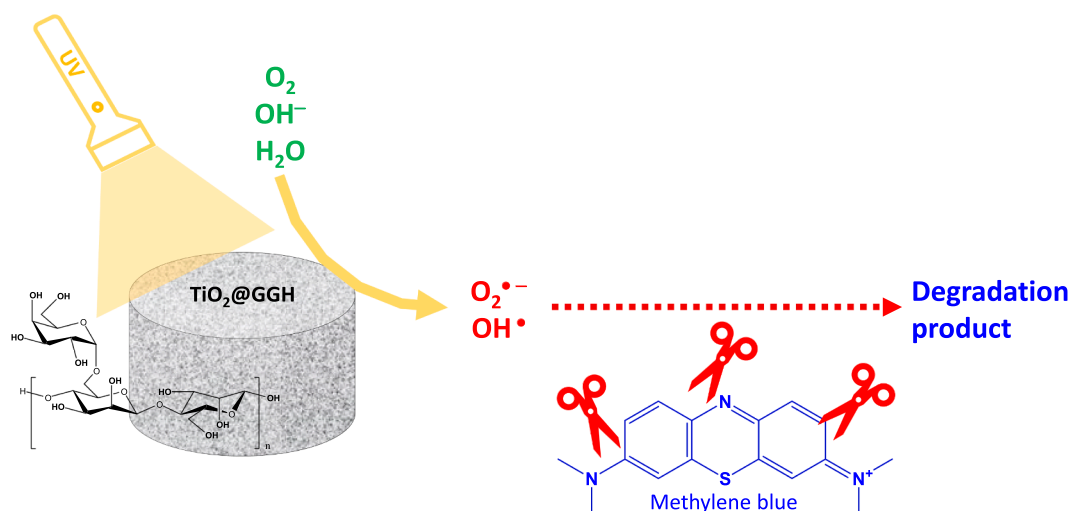
3.3. Remark on the effect of radiation

Based on the results presented above, UV radiation can enhance the MB removal rate and the adsorption capacity of GGH and TiO₂@GGH. The following trend can be observed; where the MB removal capacity decreased in the following manner TiO₂@GGH + radiation > TiO₂@GGH > GGH + radiation > GGH, while the trend of MB degradation rate: TiO₂@GGH + radiation > GGH + radiation > GGH ≈ TiO₂@GGH. It has been widely acknowledged that TiO₂ is one of the best photocatalytic materials. Upon radiation, the TiO₂ transforms oxygen (O₂), hydroxyl groups, and water (H₂O) to OH• and O₂•⁻ radicals which in charge of the MB degradation (Fig. 9) [54–58]. Besides the photocatalytic properties of the synthesized material, the removal condition (pH 10) used in this work may contribute to the generation of

Table 4
The fitting isotherm-parameters of the MB removal by GGH and TiO$_2$@GGH.

Parameter	Unit	GGH		TiO$_2$@GGH	
		Without radiation	With radiation	Without radiation	With radiation
Q_{exp}	mg g^{-1}	138.549 ± 7.386	142.726 ± 0.225	177.917 ± 2.617	184.321 ± 3.402
Langmuir (L)					
Q_L	mg g^{-1}	146.531 ± 2.797	147.487 ± 2.632	185.530 ± 2.680	198.606 ± 2.637
K_L	mg L^{-1}	0.105 ± 0.009	0.124 ± 0.009	0.120 ± 0.007	0.095 ± 0.005
R^2		0.991	0.991	0.991	0.993
RSS		137.206	118.408	143.831	106.548
Freundlich (F)					
K_F	L g^{-1}	36.830 ± 5.301	40.972 ± 5.207	57.559 ± 7.049	54.334 ± 6.930
$1/n_F$		0.281 ± 0.034	0.267 ± 0.031	0.236 ± 0.029	0.265 ± 0.031
R^2		0.922	0.915	0.899	0.912
RSS		1145.766	1092.898	1544.827	1325.220
Sips (S)					
Q_S	mg g^{-1}	156.926 ± 5.527	155.824 ± 5.506	185.327 ± 5.555	199.799 ± 6.318
n_S	L g^{-1}	0.831 ± 0.059	0.858 ± 0.067	1.004 ± 0.101	0.982 ± 0.084
K_S		0.132 ± 0.012	0.147 ± 0.015	0.119 ± 0.021	0.098 ± 0.015
R^2		0.995	0.993	0.989	0.992
RSS		64.960	75.134	143.798	105.867
Redlich-Peterson (RP)					
K_{RP}	L g^{-1}	18.83 ± 2.332	22.14 ± 2.175	23.081 ± 2.695	19.775 ± 2.087
a_{RP}	L mg^{-1}	0.173 ± 0.044	0.199 ± 0.040	0.132 ± 0.035	0.107 ± 0.027
β		0.939 ± 0.029	0.940 ± 0.023	0.987 ± 0.031	0.984 ± 0.032
R^2		0.993	0.993	0.990	0.993
RSS		89.120	59.744	140.503	102.878

more radical species; more OH$^-$ groups occurred when the system was maintained at pH 10. Upon UV radiation, they are readily transformed into OH$^\bullet$ which may attack and cleave the thiazine group of MB [56–59]. These suggest that both synthesized material and the established condition used in this study generate a synergistic effect for the efficient removal of MB in an aqueous solution.

3.4. Recyclability and comparison study

Fig. 10 shows the recycling performance of GGH and TiO$_2$@GGH for MB removal in the presence of UV radiation. The MB removal efficiency of GGH and TiO$_2$@GGH respectively maintained as high as 78.2% and 79.3% after five adsorption-desorption cycles, thus verifying that the prepared adsorbents have good recyclability.

Table 5 shows the adsorption performance of some polysaccharide-based hydrogels and hydrogel composites toward various dyes. The adsorption capacity of GGH and TiO$_2$@GGH was much higher than those of similar composite hydrogels derived from GG, especially toward MB —i.e., the experimental adsorption capacity is 1.7–2.3 times higher than GG/poly(acrylic acid-aniline) hydrogel, and 7.2–9.6 times higher than GG/acrylamide/octadecyl hydrogel.

4. Conclusion

Modification of guar gum hydrogel (GGH) by the addition of TiO$_2$ particles produced composite adsorbent with photodegradation ability. The successful grafting of TiO$_2$ particles in the GGH structure has been confirmed by using SEM-EDX and XPS analysis. The incorporation of TiO2 does not influence the porosity, thermal stability, and mechanical
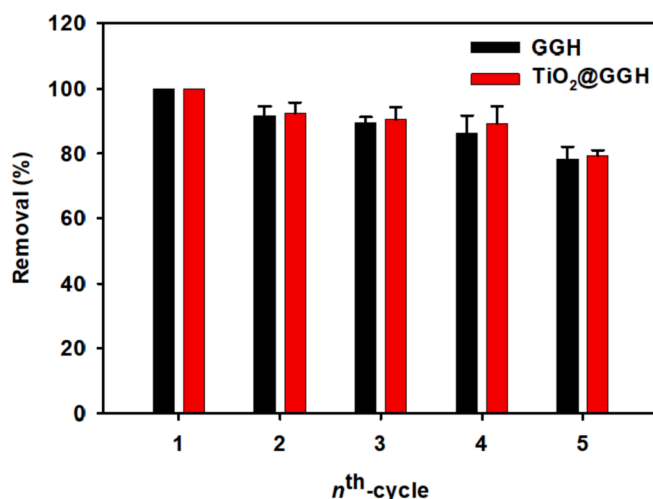

Fig. 10. Removal percentage of MB by GGH and TiO$_2$@GGH in different cycles, with the presence of UV radiation.

Fig. 9. Possible mechanism during MB photocatalytic degradation by TiO$_2$@GGH.

Table 5

Adsorption performance of come polysaccharide-based hydrogels against dyes.

Hydrogel	Adsorption system		Adsorption capacity (mg g^{-1})		Ref.
	Adsorbate[a]	Condition	Experimental	Theoretical (model)	
GG/poly(acrylic acid-aniline)	MB	pH = 10 T = r.t.	~80[b]	102.77 (P2O)	[60]
GG/polyacrylamide	CV AB	pH = 7	~14[b] (CV) ~31[b] (AB)	100 (Lang) 12 (Lang)	[61]
GG/borax	AB	pH = 9 T = r.t.	94.30 (%removal)	n.a.	[62]
GG/acrylamide/octadecyl methacrylate	MB	n.a.	19.3	n.a.	[63]
Gum ghatti/TiO$_2$	MB	pH = 7 T = 45 °C	~1450[b]	1305.5 (Lang)	[64]
Alginate/acrylic acid/TiO$_2$	MV	pH = 7 T = 45 °C	~913[b]	1156.6 (Lang)	[65]
Xanthan gum/TiO$_2$	GV	pH = 8–9	n.a.	502 (Lang)	[66]
Chitosan/sodium dodecyl sulfate		pH = 6 T = 30 °C	~199	193.16 (Lang)	[67]
Ti$_3$C$_2$T$_x$/alginate (T = OH, O, F)	MB	pH = 7 T = 25 °C	~90.5[b]	92.17 (Lang)	[68]
Cellulose/carrageenan/TiO$_2$	MB	pH = 7 T = 25 °C	115.3	n.a.	[69]
GG	MB	pH = 10 T = 30 °C	138.55[c] 142.73[d]	146.53[c] (Lang) 149.49[d] (Lang)	This work
GG/TiO$_2$	MB	pH = 10 T = 30 °C	177.92[c] 184.32[d]	185.53[c] (Lang) 198.61[d] (Lang)	This work

[a] MB = methylene blue, CV = crystal violet, AB = Azure B, AD = Aniline blue, MV = methyl violet, GV = Gentian violet

[b] The value was approximated through curve reading from the available data in the cited literature.

[c] Adsorption capacity without radiation.

[d] Adsorption capacity with radiation.

properties of the resultant hydrogels as determined by using FTIR, XRD, N$_2$ sorption, MIP, cyclic test, and TG/DTA methods. Similar to GGH, TiO$_2$@GGH may function as the adsorbent for MB removal via its adsorption ability. Superior to GGH, the TiO$_2$@GGH exhibited a photodegradation ability in the presence of UV radiation treatment which synergistically enhanced its MB removal capacity. The removal of MB by the investigated adsorbent optimally happened at more alkaline pH, which is triggered by the different charges of the adsorbate and adsorbent. The instantaneous removal of MB occurred within 120 min of adsorbent-adsorbate contact. Both GGH and TiO$_2$@GGH maintained at least 75% MB removal efficiency upon repeated usage, suggesting that GG is the suitable renewable material for synthesizing value-added and tunable adsorbents.

CRediT authorship contribution statement

Shella Permatasari Santoso: Conceptualization, Methodology, Validation, Writing – original draft, Project administration, Funding acquisition. **Artik Elisa Angkawijaya:** Formal analysis, Writing – review & editing, Resources, Supervision. **Vania Bundjaja:** Investigation, Formal analysis. **Chang-Wei Hsieh:** Project administration, Writing – original draft. **Alchris Woo Go:** Formal analysis, Validation. **Maria Yuliana:** Writing – review & editing. **Hsien-Yi Hsu:** Writing – review & editing. **Phuong Lan Tran-Nguyen:** Data curation, Formal analysis. **Felycia Edi Soetaredjo:** Methodology, Resources. **Suryadi Ismadji:** Conceptualization, Supervision.

Declaration of competing interest

The authors declare no conflict of interest.

Acknowledgment

References

[1] N. Ferronato, V. Torretta, Waste mismanagement in developing countries: a review of global issues, Int. J. Environ. Res. Public Health 16 (2019) 1060, https://doi.org/10.3390/ijerph16061060.

[2] I. Sohoo, M. Ritzkowski, K. Kuchta, S.Ö. Cinar, Environmental sustainability enhancement of waste disposal sites in developing countries through controlling greenhouse gas emissions, Sustainability 13 (2020) 151, https://doi.org/10.3390/su13010151.

[3] S. Sharma, A. Bhattacharya, Drinking water contamination and treatment techniques, Appl Water Sci 7 (2017) 1043–1067, https://doi.org/10.1007/s13201-016-0455-7.

[4] B. Lellis, C.Z. Fávaro-Polonio, J.A. Pamphile, J.C. Polonio, Effects of textile dyes on health and the environment and bioremediation potential of living organisms, Biotechnol. Res. Innov. 3 (2019) 275–290, https://doi.org/10.1016/j.biori.2019.09.001.

[5] Z. Carmen, S. Daniela, Textile organic dyes – characteristics, polluting effects and separation/elimination procedures from industrial effluents – a critical overview, in: T. Puzyn (Ed.), Organic Pollutants Ten Years After the Stockholm Convention - Environmental and Analytical Update, IntechOpen Limited, London, United Kingdom, 2012, pp. 55–86.

[6] A. Alinsafi, S.L. Bonté, M.N. Pons, A. Benhammou, M.d. Motta, Effect of variability on the treatment of textile dyeing wastewater by activated sludge, Dyes Pigm. 69 (2006) 31–39, https://doi.org/10.1016/j.dyepig.2005.02.014.

[7] P. Jia, H. Tan, K. Liu, W. Gao, Removal of methylene blue from aqueous solution by bone char, Appl. Sci. 8 (2018) 1903, https://doi.org/10.3390/app8101903.

[8] P. Staroń, J. Chwastowski, M. Banach, Sorption behavior of methylene blue from aqueous solution by raphia fibers, Int. J. Environ. Sci. Technol. 16 (2019) 8449–8460, https://doi.org/10.1007/s13762-019-02446-9.

[9] A. Andreas, Z.G. Winata, S.P. Santoso, A.E. Angkawijaya, M. Yuliana, F. E. Soetaredjo, S. Ismadji, H.-Y. Hsu, A.W. Go, Y.-H. Ju, Biocomposite hydrogel beads from glutaraldehyde-crosslinked phytochemicals in alginate for effective removal of methylene blue, J. Mol. Liq. 329 (2021), 115579, https://doi.org/10.1016/j.molliq.2021.115579.

[10] S.K. Sela, A.K.M. Nayab-Ul-Hossain, S.Z. Hussain, N. Hasan, Utilization of prawn to reduce the value of BOD and COD of textile wastewater 1 (2020), 100021, https://doi.org/10.1016/j.clet.2020.100021.

[11] S. Sarkar, A. Banerjee, U. Halder, R. Biswas, R. Bandopadhyay, Degradation of synthetic azo dyes of textile industry: a sustainable approach using microbial enzymes, Water Conserv. Sci. Eng. 2 (2017) 121–131, https://doi.org/10.1007/s41101-017-0031-5.

[12] B. Azhar, A.E. Angkawijaya, S.P. Santoso, C. Gunarto, A. Ayucitra, A.W. Go, P. L. Tran-Nguyen, S. Ismadji, Y.H. Ju, Aqueous synthesis of highly adsorptive copper–gallic acid metal–organic framework, Sci. Rep. 10 (2020) 19212, https://doi.org/10.1038/s41598-020-75927-4.

[13] K. Rehman, T. Shahzad, A. Sahar, S. Hussain, F. Mahmood, M.H. Siddique, M. A. Siddique, M.I. Rashid, Effect of reactive black 5 azo dye on soil processes related to C and N cycling, PeerJ 6 (2018), e4802, https://doi.org/10.7717/peerj.4802.

[14] X. Zhou, X. Xiang, Effect of different plants on azo-dye wastewater bio-decolorization, ProcediaEnviron. Sci. 18 (2013) 540–546, https://doi.org/10.1016/j.proenv.2013.04.073.

[15] E. Forgacs, T. Cserháti, G. Oros, Removal of synthetic dyes from wastewaters: a review, Environ. Int. 30 (2004) 953–971, https://doi.org/10.1016/j.envint.2004.02.001.

[16] N. Jafari, M.R. Soudi, R. Kasra-Kermanshahi, Biodegradation perspectives of azo dyes by yeasts, Microbiology 83 (2014) 484–497, https://doi.org/10.1134/S0026261714050130.

[17] M. Solís, A. Solís, H.I. Pérez, N. Manjarrez, M. Flores, Microbial decolouration of azo dyes: a review, Process Biochem. 47 (2012) 1723–1748, https://doi.org/10.1016/j.procbio.2012.08.014.

[18] R. Khan, P. Bhawana, M.H. Fulekar, Microbial decolorization and degradation of synthetic dyes: a review, Rev. Environ. Sci. Biotechnol. 12 (2013) 75–97, https://doi.org/10.1007/s11157-012-9287-6.

[19] S. Banerjee, M.C. Chattopadhyaya, Adsorption characteristics for the removal of a toxic dye, tartrazine from aqueous solutions by a low cost agricultural by-product, Arab. J. Chem. 10 (2017) S1629–S1638, https://doi.org/10.1016/j.arabjc.2013.06.005.

[20] A.E. Angkawijaya, S.P. Santoso, V. Bundjaja, F.E. Soetaredjo, C. Gunarto, A. Ayucitra, Y.-H. Ju, A.W. Go, S. Ismadji, Studies on the performance of bentonite and its composite as phosphate adsorbent and phosphate supplementation for plant, J. Hazard. Mater. 399 (2020), 123130, https://doi.org/10.1016/j.jhazmat.2020.123130.

[21] C. Dong, Y. Wang, H. Wang, C.S.K. Lin, H.-Y. Hsu, S.-Y. Leu, New generation urban biorefinery toward complete utilization of waste derived lignocellulosic biomass for biofuels and value-added products, Energy Procedia 158 (2019) 918–925, https://doi.org/10.1016/j.egypro.2019.01.231.

[22] C.H. Mak, X. Han, M. Du, J.-J. Kai, K.F. Tsang, G. Jia, K.-C. Cheng, H.-H. Shen, H.-Y. Hsu, Heterogenization of homogeneous photocatalysts utilizing synthetic and natural support materials, J. Mater. Chem. A 9 (2021) 4454–4504, https://doi.org/10.1039/D0TA08334H.

[23] S. Thakur, B. Sharma, A. Verma, J. Chaudhary, S. Tamulevicius, V.K. Thakur, Recent approaches in guar gum hydrogel synthesis for water purification, Int. J. Polym. Anal. Charact. 23 (2018) 621–632, https://doi.org/10.1080/1023666X.2018.1488661.

[24] N.R. Singha, A. Dutta, M. Mahapatra, M. Karmakar, H. Mondal, P. K. Chattopadhyay, D.K. Maiti, Guar gum-grafted terpolymer hydrogels for ligand-selective individual and synergistic adsorption: effect of comonomer composition, ACS Omega 3 (2018) 472–494, https://doi.org/10.1021/acsomega.7b01682.

[25] L. Dai, Y. Wang, W. Li, W. Zhao, C. Duan, C. Xiong, Y. Ni, A green all-polysaccharide hydrogel platform for sensing and electricity harvesting/storage, J. Power Sources 493 (2021) 229711, https://doi.org/10.1016/j.jpowsour.2021.229711.

[26] Y. Cheng, K. Pang, X. Xu, P. Yuan, Z. Zhang, X. Wu, L. Zheng, J. Zhang, R. Song, Borate crosslinking synthesis of structure tailored carbon-based bifunctional electrocatalysts directly from guar gum hydrogels for efficient overall water splitting, Carbon 157 (2020) 153–163, https://doi.org/10.1016/j.carbon.2019.10.024.

[27] J. Maity, S.K. Ray, Enhanced adsorption of Cr(VI) from water by guar gum based composite hydrogels, Int. J. Biol. Macromol. 89 (2016) 246–255, https://doi.org/10.1016/j.ijbiomac.2016.04.036.

[28] M.F. Hamza, A. Fouda, K.Z. Elwakeel, Y. Wei, E. Guibal, N.A. Hamad, Phosphorylation of guar gum/magnetite/chitosan nanocomposites for uranium (VI) sorption and antibacterial applications, Molecules 26 (2021) 1920, https://doi.org/10.3390/molecules26071920.

[29] M. Contreras, C.D. Grande-Tovar, W. Vallejo, C. Chaves-López, Bio-removal of methylene blue from aqueous solution by galactomyces geotrichum KL20A, Water 11 (2019) 282, https://doi.org/10.3390/w11020282.

[30] A. Labena, A.E. Abdelhamid, A.S. Amin, S. Husien, L. Hamid, G. Safwat, A. Diab, A. A. Gobouri, E. Azab, Removal of methylene blue and Congo red using adsorptive membrane impregnated with dried Ulva fasciata and sargassum dentifolium, Plants 10 (2021) 384, https://doi.org/10.3390/plants10020384.

[31] Y.S. Ho, J.C.Y. Ng, G. McKay, Kinetics of pollutant sorption by biosorbents: review, Sep. Purif. Technol. 29 (2000) 189–232, https://doi.org/10.1081/SPM-100100009.

[32] Y.S. Ho, G. McKay, The kinetics of sorption of divalent metal ions onto sphagnum moss peat, Water Res. 34 (1999) 735–742, https://doi.org/10.1016/S0043-1354(99)00232-8.

[33] Y.S. Ho, G. McKay, Application of kinetic models to the sorption of copper(II) on to peat, Adsorp. Sci. Technol. 20 (2002) 797–815, https://doi.org/10.1260/026361702321104282.

[34] F.-C. Wu, R.-L. Tseng, R.-S. Juang, Initial behavior of intraparticle diffusion model used in the description of adsorption kinetics, Chem. Eng. J. 153 (2009) 1–8, https://doi.org/10.1016/j.cej.2009.04.042.

[35] L. Liu, X.-B. Luo, L. Ding, S.-L. Luo, Application of nanotechnology in the removal of heavy metal from water, in: X. Luo, F. Deng (Eds.), Nanomaterials for the Removal of Pollutants and Resource Reutilization, Elsevier, 2019, pp. 83–147.

[36] N. Ayawei, A.N. Ebelegi, D. Wankasi, Modelling and interpretation of adsorption isotherms, J. Chem. 2017 (2017) 3039817, https://doi.org/10.1155/2017/3039817.

[37] L. Holmberg, B. Lindberg, B. Lindqvist, The reaction between epichlorohydrin and polysaccharides: part 1, syntheses of some model substances with non-cyclic substituents, Carbohydr. Res. 262 (1994) 213–221, https://doi.org/10.1016/0008-6215(94)84180-2.

[38] D.R. Medjitov, L.G. Shode, G.M. Tseitlin, Composition of condensation products of bisphenol-a and epichlorohydrin, Polym. Bull. 40 (1998) 509–516, https://doi.org/10.1007/s002890050284.

[39] S.P. Santoso, A. Kurniawan, F.E. Soetaredjo, K.-C. Cheng, J.N. Putro, S. Ismadji, Y.-H. Ju, Eco-friendly cellulose–bentonite porous composite hydrogels for adsorptive removal of azo dye and soilless culture, Cellulose 26 (2019) 3339–3358, https://doi.org/10.1007/s10570-019-02314-2.

[40] A.H. Karoyo, L.D. Wilson, Physicochemical properties and the gelation process of supramolecular hydrogels: a review, Gels 3 (2017) 1, https://doi.org/10.3390/gels3010001.

[41] S. Maitia, P.S. Khillarab, D. Mishra, N.A. Nambiraj, A.K. Jaiswal, Physical and self–crosslinking mechanism and characterization of chitosan-gelatin-oxidized guar gum hydrogel, Polym. Test. 97 (2021), 107155, https://doi.org/10.1016/j.polymertesting.2021.107155.

[42] P. Krishnan, M. Liu, P.A. Itty, Z. Liu, V. Rheinheimer, M.-H. Zhang, P.J. M. Monteiro, L.E. Y, Characterization of photocatalytic TiO2 powder under varied environments using near ambient pressure X-ray photoelectron spectroscopy, Sci. Rep. 7 (2017) 43298, https://doi.org/10.1038/srep43298.

[43] M.C. Biesinger, L.W. Lau, A.R. Gerson, R.S.C. Smart, Resolving surface chemical states in XPS analysis of first row transition metals, oxides and hydroxides: Sc, Ti, V, Cu and Zn, Appl. Surf. Sci. 257 (2010) 887–898, https://doi.org/10.1016/j.apsusc.2010.07.086.

[44] F. Anjum, S. Gul, M.I. Khan, M.A. Khan, Efficient synthesis of palladium nanoparticles using guar gum as stabilizer and their applications as catalyst in reduction reactions and degradation of azo dyes, Green Process. Synth. 9 (2019) 63–76, https://doi.org/10.1515/gps-2020-0008.

[45] D. Mudgil, S. Barak, B.S. Khatkar, X-ray diffraction, IR spectroscopy and thermal characterization of partially hydrolyzed guar gum, Int. J. Biol. Macromol. 50 (2012) 1035–1039, https://doi.org/10.1016/j.ijbiomac.2012.02.031.

[46] J. Wang, P. Somasundaran, Study of galactomannose interaction with solids using AFM, IR and allied techniques, J. Colloid Interface Sci. 309 (2007) 373–383, https://doi.org/10.1016/j.jcis.2006.10.086.

[47] Y. Lu, P. Tao, N. Zhang, S. Nie, Preparation and thermal stability evaluation of cellulose nanofibrils from bagasse pulp with differing hemicelluloses contents, Carbohydr. Polym. 245 (2020), 116463, https://doi.org/10.1016/j.carbpol.2020.116463.

[48] S. Nie, J Mo, Y. Zhang, G. Xiong, S. Wang, Ultra-high thermal-conductive, reduced graphene oxide welded cellulose nanofibrils network for efficient thermal management, Carbohydr. Polym. 250 (2020), 116971, https://doi.org/10.1016/j.carbpol.2020.116971.

[49] J.J. Salazar-Rabago, R. Leyva-Ramos, J. Rivera-Utrilla, R. Ocampo-Perez, F. J. Cerino-Cordova, Biosorption mechanism of methylene blue from aqueous solution onto white pine (Pinus durangensis) sawdust: effect of operating conditions, sustain. Environ. Res. 27 (2017) 32–40, https://doi.org/10.1016/j.serj.2016.11.009.

[50] J.J.M. Órfao, A.I.M. Silva, J.C.V. Pereira, S.A. Barata, I.M. Fonseca, P.C.C. Faria, M. F.R. Pereira, Adsorption of a reactive dye on chemically modified activated carbons—influence of pH, J. Colloid Interface Sci. 296 (2006) 480–489, https://doi.org/10.1016/j.jcis.2005.09.063.

[51] A.A. Moosa, A.M. Ridha, N.A. Kadhim, Use of biocomposite adsorbents for the removal of methylene blue dye from aqueous solution, Am. J. Mater. Sci. 6 (2016) 135–146, https://doi.org/10.5923/j.materials.20160605.03.

[52] F. Gorzin, M.M.B.R. Abadi, Adsorption of Cr(VI) from aqueous solution by adsorbent prepared from paper mill sludge: kinetics and thermodynamics studies, Adsorp.Sci. Technol. 36 (2018) 149–169, https://doi.org/10.1177/0263617416686976.

[53] J.S. Piccin, T.R.S.A. Cadaval, L.A.A.d. Pinto, G.L. Dotto, Adsorption isotherms in liquid phase: experimental, modeling, and interpretations, in: A. Bonilla-Petriciolet, D.I. Mendoza-Castillo, H.E. Reynel-Ávila (Eds.), Adsorption Processes for Water Treatment and Purification, Springer, Switzerland, 2017, pp. 19–51.

[54] Inamuddin, Xanthan gum/titanium dioxide nanocomposite for photocatalytic degradation of methyl orange dye, Int. J. Biol. Macromol. 121 (2019) 1046–1053, https://doi.org/10.1016/j.ijbiomac.2018.10.064.

[55] N. Xu, Z. Shi, Y. Fan, J. Dong, J. Shi, M.Z.C. Hu, Effects of particle size of TiO2 on photocatalytic degradation of methylene blue in aqueous suspensions, Ind. Eng. Chem. Res. 38 (1999) 373–379, https://doi.org/10.1021/ie980378u.

[56] C. Xu, G.P. Rangaiah, X.S. Zhao, Photocatalytic degradation of methylene blue by titanium dioxide: experimental and modeling study, Ind. Eng. Chem. Res. 53 (2014) 14641–14649, https://doi.org/10.1021/ie502367x.

[57] E.M. Cuerda-Correa, M.F. Alexandre-Franco, C. Fernández-González, Advanced oxidation processes for the removal of antibiotics from water.An Overview 12 (2020) 102, https://doi.org/10.3390/w12010102.

[58] Y. Nosaka, A. Nosaka, Understanding hydroxyl radical (•OH) generation processes in photocatalysis, ACS Energy Lett. 1 (2016) 356-259, https://doi.org/10.1021/acsenergylett.6b00174.

[59] F. Azeez, E. Al-Hetlani, M. Arafa, Y. Abdelmonem, A.A. Nazeer, M.O. Amin, M. Madkour, The effect of surface charge on photocatalytic degradation of methylene blue dye using chargeable titania nanoparticles, Sci. Rep. 8 (2018) 7104, https://doi.org/10.1038/s41598-018-25673-5.

[60] R. Sharma, S. Kalia, B.S. Kaith, M.K. Srivastava, Synthesis of guar gum-acrylic acid graft copolymers based biodegradable adsorbents for cationic dye removal, Int. J. Plast. Technol. 20 (2016) 294–314, https://doi.org/10.1007/s12588-016-9156-1.

[61] J.N. Hiremath, B. Vishalakshi, Evaluation of a pH-responsive guar gum-based hydrogel as adsorbent for cationic dyes: kinetic and modelling study, Polym. Bull. 72 (2015) 3063–3081, https://doi.org/10.1007/s00289-015-1453-x.

[62] N. Thombare, U. Jha, S. Mishra, M.Z. Siddiqui, Borax cross-linked guar gum hydrogels as potential adsorbents for water purification, Carbohydr. Polym. 168 (2017) 274–281, https://doi.org/10.1016/j.carbpol.2017.03.086.

[63] J. Duan, Y. Gao, Y. Huang, L. Li, J. Jiang, Preparation and characterization of a high strength self-repairing galactomannan hydrogel, Bioresources 14 (2019) 9853–9866.

[64] H. Mittal, S.S. Ray, A study on the adsorption of methylene blue onto gum ghatti/TiO2 nanoparticles-based hydrogel nanocomposite, Int. J. Biol. Macromol. 88 (2016) 66–80, https://doi.org/10.1016/j.ijbiomac.2016.03.032.

[65] S. Thakur, O. Arotiba, Synthesis, characterization and adsorption studies of an acrylic acid-grafted sodium alginate-based TiO2 hydrogel nanocomposite, Adsorp. Sci. Technol. 36 (2017) 458–477, https://doi.org/10.1177/0263617417700636.

[66] D.G. Njuguna, H. Schönherr, Xanthan gum hydrogels as high-capacity adsorbents for dye removal, ACS Appl. Polym. Mater. 3 (2021) 3142–3152, https://doi.org/10.1021/acsapm.1c00343.

[67] S. Chatterjee, T. Chatterjee, S.-R. Lim, S.H. Woo, Adsorption of a cationic dye, methylene blue, on to chitosan hydrogel beads generated by anionic surfactant gelation, Environ. Technol. 32 (2011) 1503–1514, https://doi.org/10.1080/09593330.2010.543157.

[68] Z.-H. Zhang, J.-Y. Xu, X.-L. Yang, MXene/sodium alginate gel beads for adsorption of methylene blue, Mater. Chem. Phys. 260 (2021), 124123, https://doi.org/10.1016/j.matchemphys.2020.124123.

[69] S. Jo, Y. Oh, S. Park, E. Kan, S.H. Lee, Cellulose/carrageenan/TiO2 nanocomposite for adsorption and photodegradation of cationic dye, biotechnol, Bioprocess Eng. 22 (2017) 734–738, https://doi.org/10.1007/s12257-017-0267-0.